# Empirical forward scattering phase functions from 0.08 to 16 deg. for randomly shaped terrigenous 1-21 μm sediment grains

**Y. C. Agrawal**[*] **and Ole A. Mikkelsen**
*Sequoia Scientific, Inc., 2700 Richards Road, Bellevue, WA 98005*
*\*Corresponding author: yogi.agrawal@sequoiasci.com*

**Abstract:** We present in-water forward scattering phase functions covering the angle range 0.08 to 16° for 19 narrow-sized dispersions of randomly shaped sediment grains. These dispersions cover particle size range from 1 to 20 microns. These phase functions offer a realistic alternative to Mie theory. Qualitatively, (i) the magnitude of phase functions at the smallest angles for equal size spheres and randomly shaped particles are nearly equal; (ii) the oscillations predicted by Mie theory for spheres disappear for random shaped grains, and (iii) the tendency of phase functions of large spheres to merge at large angles is also seen with randomly shaped grains. The data are also provided in tabulated form.

## References and links

1. Y. C. Agrawal, A. Whitmire, O. A. Mikkelsen and H. C. Pottsmith, "Light scattering by random shaped particles and consequences on measuring suspended sediments by Laser Diffraction" J. Geophys. Res. **113**, (2008).
2. E. Boss, W. H. Slade, M. Behrenfeld, and G. Dall'Olmo, "Acceptance angle effects on the beam attenuation in the ocean" Opt. Express **17**, 1535-155 (2009).
3. Y. C. Agrawal and H. C. Pottsmith, "Instruments for particle size and settling velocity observations in sediment transport," Mar. Geol. **168**, 89-114 (2000).
4. E. D. Hirleman, "Optimal scaling of the inverse Fraunhofer Diffraction particle sizing problem: the linear system produced by Quadrature," Part. Charact. **4**, 128-133 (1987).
5. W. H. Slade and E. S. Boss, "Calibrated near-forward volume scattering function obtained from the LISST particle sizer," Opt. Express **14**, 3602-3614 (2006).
6. H. C. Van de Hulst, *Light Scattering by Small Particles*, (Dover, New York, 1981), pp. 470.
7. R. Jones, "Fraunhofer diffraction by random irregular particles" Part. Charact. **4**, 123-127 (1987).
8. Y. C. Agrawal, "The optical volume scattering function: temporal and vertical variability in the water column off the New Jersey coast," Limnol. Oceanogr. **50**, 1787-1794 (2005).

## 1. Introduction

This work provides empirical data for synthesis of forward scattering phase functions of terrigenous sediments, suspended in water. Although progress in theoretical modeling of forward scattering now permits calculations of this phase function for small sizes (up to 6 μm, we are not aware of physical measurements of size-sorted grains that may be used for verification of models. A review of current state of experimental data was presented by [1]. We have previously published characteristic scattering functions (CSF) in a form useful to particle sizing application by the laser diffraction method [1]. The CSF's are characteristic shapes of light scattered by particles on a set of ring detectors used therein (see later). Although the CSF is related to scattering phase functions, these were not presented. The present data are directed specifically for the community concerned with the inherent optical properties of sediment laden water. The data should be useful in constructing volume scattering functions and beam spread functions of water from knowledge of size distribution

of suspended particles when the particles are of terrigenous origin. Besides presenting scattering phase functions, we are also extending the reported particle sizes down to 1 micron, and angle range to 16-degrees, twice the previous range. Only sediments of homogeneous density are considered. Randomly shaped grains exclude plate-like clay particles, which have obvious preferred directions. The sediments analyzed were size-sorted from a parent population of ISO-12301-1 standard material which is derived from Arizona rock samples.

The phase functions were measured in a density-stratified settling column filled with an alcohol-water mixture. The column is calibrated against powders sized with Coulter Counters. The powders are weakly rust colored and when viewed under a microscope, appear mostly transparent, with only a weak absorption. For this reason, we assume the imaginary part of the refractive index to be negligibly small. A crude upper bound can be estimated as follows. Light intensity seen through a 100 micron grain appears attenuated to, say, $1/e^2$. Crudely, this represents $\exp(-4\pi dm/\lambda)$ where $d$ is diameter, $\lambda$ is wavelength, and $m$ is the imaginary index. It follows that $m \sim 0.001$. From Mie theory, then attenuation coefficient $c$ and scattering coefficient $b$ are then equal to better than experimental accuracy. Therefore, normalization with $c$ is used for converting volume scattering functions to phase functions.

## 2. Methods

We have described the method earlier in [1], so that it is only briefly repeated here for completeness. The empirical method consists of sorting particles in narrow size distributions. The separation is done as particles settle in a 10 cm tall column, as shown in Fig. 1. The column is filled with a continuously varying mixture of alcohol and water.
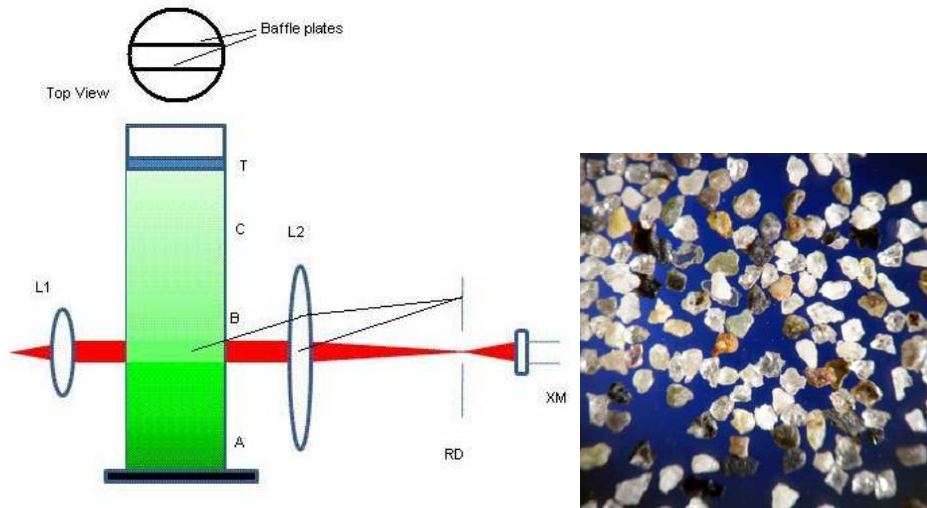


Fig. 1. LISST-ST schematic (left). *Left to right*: beam from a laser diode is collimated by lens L1, passes through the scattering volume and is focused by receive lens L2. Multi-angle scattered light is sensed by ring detectors (RD), while attenuated laser beam power is measured by photo-diode XM. The layers in order of decreasing density are marked A,B, C and the particles are inserted in top layer. (right) an image of grains, 25-32 micron dia., that were sorted for illustrating shape.

Only a small portion of this column where an 8 mm diameter laser beam passes (see below) is not density stratified, it is filled with a well-mixed intermediate density solution. This is a ~10mm thick region. Stratification is achieved by a fairly well-known method for the purpose. This involves pouring water into a well-stirred beaker containing gin. The mixture overflows into a tube that discharges the mixture at the bottom of the column. With passage of time, the

beaker density increases as the water column rises, thus filling the bottom with denser mixture. The bottom of the column is nearly pure, filtered water, whereas the top is about 30% gin. The mixture is prepared with food coloring added to the water. This coloring does not add scattering as it dissolves fully. The coloring renders stratification recognizable – low density surface layers being light colored and lower layers being darker.

The settling column diameter is 5 cm, but a pair of vertical baffle plates are placed 1 cm apart inside the column, parallel to and above the laser beam (see top view, Fig. 1). These baffle plates act to further suppress turbulence that may be driven by air drafts in the laboratory. The baffle plates reach only as far down as about 2.5 cm above the laser, thus not interfering with scattered light. The cross-section of the space between the plates is 5 cm x 1 cm. Particles were added as follows. A sample of the powder (AC Fine, i.e. ISO-12301) was dispersed in pure gin and shaken vigorously. Gin naturally discourages floc formation, so that the powder breaks up into individual grains. A small volume (~1 cc) of this suspension, with an obviously lower density, was introduced carefully with near-zero vertical momentum at the surface of the column, forming a clear, identifiable buoyant layer at the top, about 2 mm thick. From this layer, particles rained down to the laser beam. Large, fast settling particles reach the horizontal laser beam first, while smaller, slower ones arrive later. Thus, particle size is defined by settling velocity. For this to be true, particles must be of uniform density, and of identical shape factors in so far as shape affects low Reynolds number settling. The column kinematic viscosity was measured by dropping known-size glass beads. In comparison to settling in water, the Stokes settling velocity for these glass beads in the stratified column is altered solely by the changed viscosity. The relative arrival time yields the viscosity. Our measurement for the column gave an average column viscosity as 1.2 centi-stokes. Again, in a manner similar to [1], the slowing of random-shaped particles due to the combined effect of higher viscosity and shape effects was established using a starting suspension of a mixture of 2 powders, one containing particles from 2-6 microns and another from 6-11 microns (10 and 90% cumulative distribution points). These powders were obtained from PTI Inc. Their size distributions were reported by PTI with Coulter Counters. It is implied that size is thus defined by the Coulter size of particles throughout this paper. The shape of these particles is illustrated in Fig. 1 on right.

Multi-angle forward scattering was measured using a LISST-ST, type-B instrument (manuf. Sequoia Scientific, Inc., USA). This is a submersible field instrument. A 670nm laser beam exits one window to illuminate particles in water. The laser beam and scattered light enter a second 'receive side' window. A receiving lens of focal length $f$ = 60 mm focuses the incident light so that the beam itself focuses to a spot, passing through a 75 micron hole at center of a set of circular ring detectors. Power of the attenuated beam passing through the hole is measured with a photo-diode. This constitutes a measure of beam-attenuation. The hole size defines an 'acceptance angle' for scattered light of atan(37.5e-3/60), or 0.036 degrees in air, i.e. 0.027 degress in water. The acceptance angle is significant because intense forward scattered light is also transmitted through the tiny hole, thus creating the impression of a stronger laser beam, or equivalently, a smaller beam attenuation coefficient $c$. The goodness of the measurement of $c$ with these instruments has recently become established [2]. The scattered light originating at a particular angle anywhere along the beam reaches a point on the focal plane of the lens that subtends the same angle to the optics axis, see Fig. 1. Light at any point on the focal plane at radius $r$ thus represents scattering all along the beam (in air) at angle atan($r/f$). There are 32 concentric ring detectors in the lens focal plane, each covering a 60-deg. azimuthal arc. The ring detector radii increase in a geometric progression, each being $\rho$ ($\rho$ =1.1809) times the previous. In this manner, ring detector number n (1 being the innermost ring) measures scattering over angles atan($\rho^{n-1} r_o/f$) to atan($\rho^n r_o/f$). These angles are defined in air. The corresponding angles in water are corrected through Snell's law. More details of the instrumentation have been published earlier [1, 3].

We have selected a subset of 19 size classes out of 32 logarithmically spaced size classes

from 1 to 200 microns. The lowest size-class is 1 to 1.1809 microns, the next one from 1.1809 to $1.1809^2$ microns, and so on. These sizes are selected based on particle sizing considerations, and are almost exactly $2^{1/4}$ apart, which is recognizable to geologists as a ¼-ɸ spacing in sizes. The size-classes are listed across the top row of Table-1.

The reporting of phase functions requires absolute calibration of the radiant sensitivity of ring detectors. Again, as described by [1], this response in Amp/Watt is determined with NIST traceable standard as follows. With the ring detector removed from this assembly, a weak, ~1 μW laser beam, whose power is measured precisely with an NIST standard laser power meter, is sequentially focused onto several of the larger rings. The output of each ring is amplified with a current amplifier (I-V converter, converting current to voltage). This amplifier converts 1μA to 1V with 1% accuracy. A mean sensitivity of all silicon rings is constructed from these multiple estimates. The resulting value was 0.49A/W with a 4% standard error, compared to manufacturer specification of 0.47A/W. Once the laser power entering water is known (also calibrated to NIST standard) and the scattered light power is measured, the phase function is computed following Agrawal, et al. (2005), Eq. 14. This computation applies the radiant sensitivity (A/W) of the detectors, the solid angle represent by each ring (including compensation for the fact that each ring covers only $60^o$ arc), and the calibration of laser power transmission sensor. The consistency of data and Mie calculations was demonstrated in [1] [also see Fig. 4].

As noted, the phase functions thus measured are averages over the angle covered by each ring detector. Consequently, fine structure in scattering that is finer than detector ring widths would be attenuated. Is this significant? Do the phase functions reported here therefore lose the fine structure detail? We consider this question next as it is central to the question of if the present data cover full detail of the phase function.

Typical Mie scattering phase functions from spheres of 3 distinct sizes, as seen by ring detectors, are shown in Fig. 2. We call these the characteristic scattering functions (CSF). Note first that as seen by ring detectors, the amplitude of the main peak of CSF's for all sizes is equal for particles whose scattering efficiency is 2. The main forward scattering lobe and the second lobe of Mie scattering are clearly resolved by the ring detectors. Indeed, the logarithmic spacing of the ring radii was the result of an optimization of detector geometry in particle sizing theory. With these log-spaced ring detectors the forward scattering pattern for any size is identical. When plotted against ring detector sequential numbers, the main scattering lobe of Mie theory transforms to a main scattering peak. The entire pattern shifts left or right depending on if particle size is larger or smaller, respectively. Thus, the precise location of the pattern represents particle size. When a dispersion of particles is present, the resulting summed pattern is a convolution of this characteristic pattern and the size distribution. It was the optimization of this deconvolution to recover size distribution that produced the logarithmic spacing of ring detectors [4]. So, the first two lobes of Mie scattering from *any* size particles are clearly observable by ring detectors. By inference, if no secondary maximum similar to Mie theory is observed by the ring detectors, and within the self-consistency of the data, it can be safely concluded that the rings represent the true structure of scattering, and that no secondary maxima in scattering exist in the process being measured. We shall return to this after presentation of data.

The CSF's of Fig. 2 merge at the larger ring detectors, reaching a common value. This is a consequence of the fact that scattering at these large angles, and from large spherical particles follows geometric optics laws. We shall show that randomly shaped particles also show a tendency to this common tail of the CSF's.
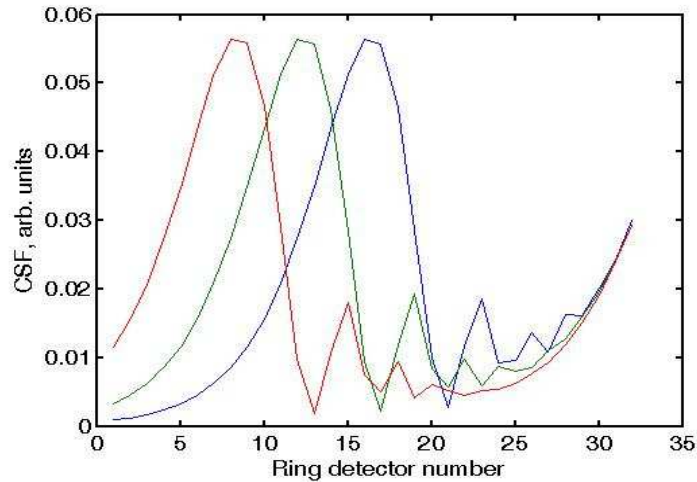
Fig. 2. CSF's of 3 distinct sized particles according to Mie theory; red: 61.7, green: 31.9 and blue: 16.5 μm.

A consequence of using ring detectors is that for very small particles, which have their characteristic peak on the (outer) larger ring detectors, the (inner) small rings see very little light. At these small rings, therefore, the data are noisy. In this case, we replace the
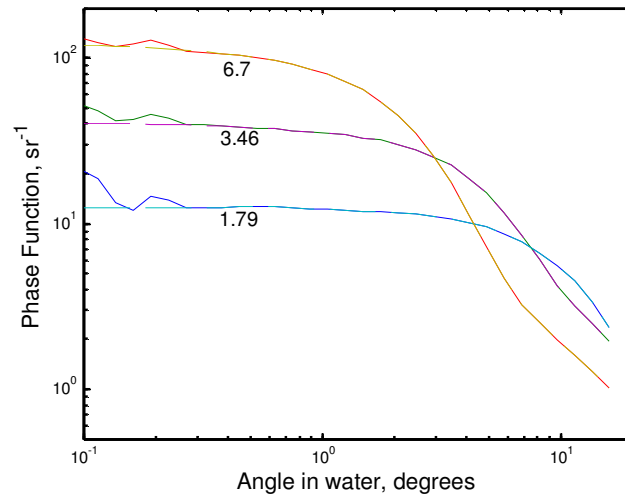


Fig. 3. Phase functions as measured (solid line), and replaced values at small angles (broken line). Three sizes are shown for clarity, size increases from lowest curve to top.

actually measured values as follows. Since the scattering function is symmetric about 0-deg, we construct a scattering phase function covering the same, but negative angular range (i.e. rings -1 to -32), simply by reflecting the measured pattern about the ordinate axis. A second order fit between 'good data' on either side of the y-axis is then found to replace noisy data at rings 1-4. An example of such data manipulation is shown in Fig. 3.We next consider the question of how we know that the settling column was completely still, i.e. free from convective motions, so that we can depend on settling velocity to define size as small as 1 micron. We shall see (Fig. 5) from the data that the measured CSF's shift in a regular pattern from right to left, as finer particles fall to the laser beam. The approximate similarity between the measurement and Mie theory for equivalently sized particles, Fig. 4, particularly for the 1

μm particles, offers further validation that particle settling velocity was not biased significantly by convection currents in the column. It is worth noting that for this statement to be true, convective motions must be much weaker than the settling velocity of the smallest particles (1-micron) of concern here. The settling velocity for these particles, accounting for higher viscosity than water and for shape effect, was 1.4-microns/second.
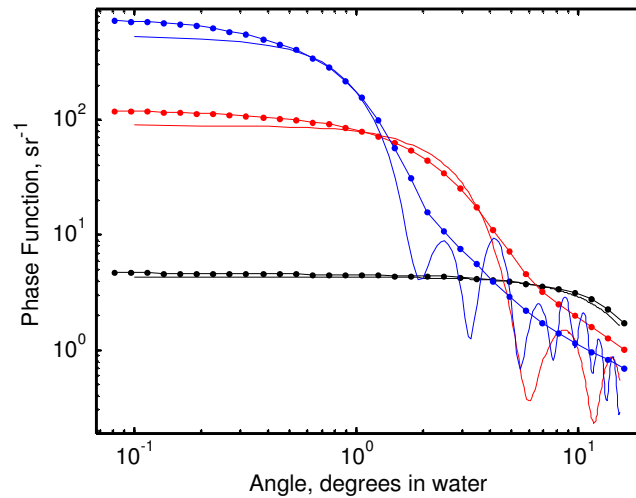


Fig. 4. Measured phase functions for random grains (.-) vs. Mie calculations (solid) for spheres of refractive index 1.5 in water; diameters: 1.1 (black), 6.7 (red), and 18.1 μm (blue).

## 3. Results

 As we have provided calibration data comparing Mie theory and measurements with this instrument for the settling column in earlier papers [1,5], we do not repeat these here, but instead display the full set of phase functions. Although the phase functions can be extracted from our data for size ranges as narrow as ~4%, we present only data for size fractions that are 18% wide. [The 4% figure comes from the width of the laser beam 0.8 cm, compared to height of settling column (10cm), and the squared relationship between size and settling velocity.]

Figure 5 shows the measured CSF for 19 log-spaced size classes, as seen by the ring detectors. These curves represent net scattering in digital counts, smoothed by a 2-point top-hat filter. No other data manipulation has been carried out. The curve peaking to the extreme left is for the largest size class, and vice versa. Viewing the CSF curves from right to left (small to large sizes) the magnitude of peaks first increases as particle size increases from 1 micron, then declines with further increase in grain size. This is similar, but not necessarily identical to a higher than 2 scattering efficiency for small particles, see [6], p.151. The 10 left-most peaks also underscore the nearly equal magnitudes of the CSF curves for large particles, similar to Mie theory, Fig. 2. Note the extremely small values of the CSF curves for small rings, where measurement error can be important, which required smoothing shown in Fig. 3.
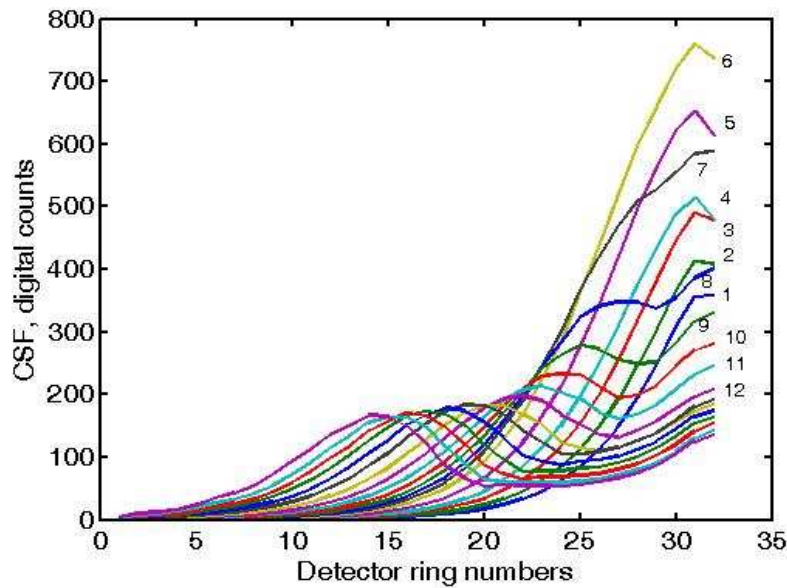
Fig. 5. The characteristic scattering functions of randomly shaped grains as seen by the ring detectors, for all 19 size classes. Numbers on curves indicate size classes. Sizes above 12 are sequential below the curve labeled 12.

We present the fully calibrated phase functions in graphic, Fig. 6, and tabular, Table I, forms, along with the sizes and angles. The angles are values in water. The highest peak in Fig. 6 is for the largest size. As is seen with Mie theory, so also here, the magnitude of the largest 11 phase functions at extreme left decrease systematically from the top by nearly fixed factors. This follows from the sizes decreasing by fixed factor of 1.1809, and that this is the region of scattering where diffraction dominates, i.e. the phase function magnitude scales with diameter squared. As sizes decrease further, the phase function magnitudes at the left edge decrease less regularly, representing the region where scattering efficiency departs from 2.

At the larger end of scattering angles, the phase functions for all sizes show a smooth, gradual decline. No hint of a secondary maximum is seen on any of these curves, as was seen for spheres in Fig. 2. An intuitive explanation for the absence of the secondary maxima draws on shading in telescopes. Diffraction was known to produce rings around images of stars due to the abrupt edge of the light gathering principal lens or mirror. By 'shading' the edges, i.e. reducing the transmission gradually to zero at the edge, the diffraction rings were suppressed. The same was reported in a diffraction-only model of light scattering through random-shaped apertures by [7]. They showed a steady weakening and eventual disappearance of secondary maxima in scattering from apertures with increasing departure from circularity. Thus it seems appropriate to suggest that roughness of random shaped particles erases secondary maxima and further oscillations that are typical of Mie scattering. Figure 6 also shows a tendency of the phase functions for larger particles to merge to common values at the larger angles. We have noted earlier that this is the region of angles where large spherical particles can be well described by geometric optics. Apparently, the same holds true for randomly shaped particles.
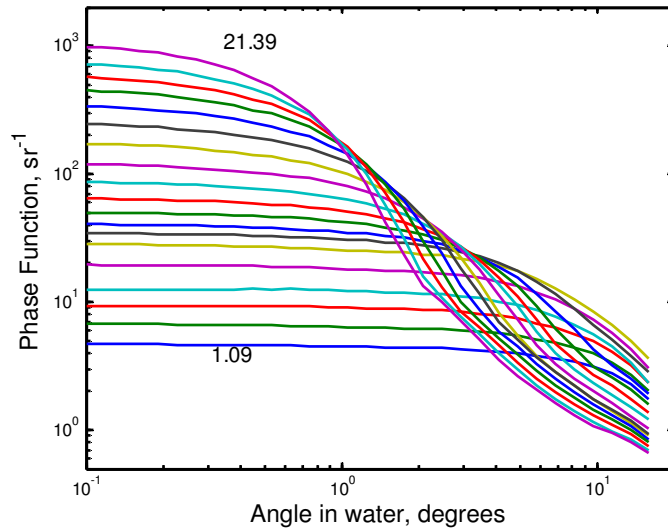
Fig. 6. Phase functions; numbers on top and bottom curves indicate grain diameters in microns.

## 4. Summary

Using a density-stratified settling column and a multi-angle scattering instrument LISST, we have constructed the phase functions of 19 log-spaced sizes from 1 to 20 microns, and over the angle range from 0.08 to 16 degrees. The principal difference between Mie theory and scattering by random shaped natural grains is in the absence of the oscillations seen with the former, which disappear for the latter. The main scattering peak of the two is similar. The amplitudes are similar. The large angle tails of the phase functions for randomly shaped grains exhibit a tendency to merge to a common value for large particles, similar to spheres, which is known to be due to the validity of geometric optics there. These phase functions can be used to replace Mie theory for purposes of estimating small-angle forward scattering from terrigenous particles of any size distribution within 1 to 20 microns. Such situations arise in estuaries and coastal seas with significant river input, such as the Columbia river discharge into the Pacific, or Mississippi plume in the Gulf of Mexico, etc. They are relevant to understanding the volume scattering functions of oceanic and river waters [8].

These data are for terrigenous particles and at wavelength 0.670 nm. The refractive index of these particles is unknown to us. The phase functions of sediment grains from other sources may be different due to refractive index changes. A limited view of variability associated with refractive index was included in [1], where it was seen that this effect was small, compared to the contrast between spheres and random shapes.

These data ignore the polarization properties of the scattered light, on the assumption that with diffraction still being the dominant part of light scattering, the scattered light maintains the polarization of the incident light. However, this is an open question and bears future investigation.

**Table – 1,** Phase functions (units: sr⁻¹) of randomly shaped grains from 1.09 to 21.39 micron sizes. Top row shows size, and first column on left shows angles in degrees.

| angle/size | 1.09 | 1.28 | 1.51 | 1.79 | 2.11 | 2.49 | 2.93 | 3.46 | 4.09 | 4.82 | 5.69 | 6.71 | 7.92 | 9.35 | 11.03 | 13.02 | 15.36 | 18.13 | 21.39 |
|---|---|---|---|---|---|---|---|---|---|---|---|---|---|---|---|---|---|---|---|
| 0.08 | 4.69 | 6.79 | 9.19 | 12.36 | 19.48 | 28.28 | 34.41 | 40.48 | 49.78 | 64.29 | 86.26 | 119.15 | 173.32 | 245.46 | 338.86 | 449.56 | 572.05 | 728.53 | 997.38 |
| 0.10 | 4.69 | 6.78 | 9.19 | 12.37 | 19.48 | 28.28 | 34.38 | 40.44 | 49.73 | 64.20 | 86.09 | 118.86 | 172.74 | 244.50 | 337.28 | 447.19 | 568.63 | 723.63 | 989.58 |
| 0.11 | 4.68 | 6.77 | 9.20 | 12.37 | 19.46 | 28.26 | 34.32 | 40.36 | 49.62 | 64.01 | 85.75 | 118.28 | 171.58 | 242.57 | 334.11 | 442.43 | 561.79 | 713.85 | 973.99 |
| 0.14 | 4.67 | 6.76 | 9.20 | 12.38 | 19.44 | 28.21 | 34.24 | 40.24 | 49.47 | 63.72 | 85.24 | 117.41 | 169.84 | 239.69 | 329.35 | 435.30 | 551.53 | 699.18 | 950.61 |
| 0.16 | 4.67 | 6.74 | 9.21 | 12.40 | 19.40 | 28.15 | 34.13 | 40.08 | 49.26 | 63.34 | 84.55 | 116.25 | 167.52 | 235.84 | 323.01 | 425.79 | 537.85 | 679.62 | 919.42 |
| 0.19 | 4.66 | 6.72 | 9.21 | 12.42 | 19.36 | 28.06 | 33.99 | 39.88 | 49.00 | 62.87 | 83.70 | 114.80 | 164.62 | 231.03 | 315.08 | 413.90 | 520.75 | 655.17 | 880.45 |
| 0.23 | 4.64 | 6.69 | 9.22 | 12.44 | 19.31 | 27.96 | 33.83 | 39.64 | 48.68 | 62.30 | 82.67 | 113.06 | 161.14 | 225.25 | 305.57 | 399.64 | 500.23 | 625.82 | 833.67 |
| 0.27 | 4.63 | 6.67 | 9.23 | 12.46 | 19.26 | 27.83 | 33.64 | 39.35 | 48.31 | 61.63 | 81.48 | 111.02 | 157.08 | 218.52 | 294.47 | 382.99 | 476.29 | 591.59 | 779.10 |
| 0.32 | 4.62 | 6.64 | 9.25 | 12.49 | 19.19 | 27.68 | 33.42 | 39.03 | 47.90 | 60.87 | 80.11 | 108.70 | 152.44 | 210.82 | 281.79 | 363.97 | 448.93 | 552.46 | 716.74 |
| 0.38 | 4.60 | 6.61 | 9.21 | 12.49 | 19.13 | 27.51 | 33.21 | 38.65 | 47.49 | 59.91 | 78.57 | 106.04 | 147.23 | 201.97 | 267.81 | 343.15 | 417.19 | 507.55 | 647.71 |
| 0.45 | 4.58 | 6.57 | 9.34 | 12.62 | 19.04 | 27.34 | 32.91 | 38.37 | 46.93 | 59.25 | 76.88 | 103.04 | 141.11 | 191.90 | 250.34 | 316.26 | 382.74 | 457.65 | 563.96 |
| 0.53 | 4.56 | 6.54 | 9.30 | 12.58 | 18.89 | 27.13 | 32.44 | 37.66 | 46.10 | 57.95 | 74.95 | 100.43 | 135.63 | 183.68 | 235.97 | 295.93 | 351.31 | 411.83 | 488.70 |
| 0.63 | 4.54 | 6.50 | 9.28 | 12.64 | 18.88 | 26.73 | 32.35 | 37.40 | 45.83 | 56.86 | 72.95 | 96.29 | 127.81 | 169.49 | 214.49 | 262.80 | 302.50 | 343.76 | 387.03 |
| 0.75 | 4.52 | 6.46 | 9.22 | 12.48 | 18.63 | 26.68 | 31.79 | 36.52 | 44.48 | 55.02 | 70.18 | 92.06 | 121.02 | 158.45 | 196.41 | 234.41 | 262.13 | 287.85 | 308.30 |
| 0.89 | 4.50 | 6.41 | 9.09 | 12.31 | 18.38 | 26.29 | 31.27 | 35.79 | 43.27 | 53.14 | 66.89 | 85.88 | 109.90 | 140.73 | 168.54 | 194.17 | 208.95 | 217.06 | 217.94 |
| 1.05 | 4.48 | 6.37 | 8.97 | 12.14 | 18.06 | 25.88 | 30.49 | 34.75 | 41.62 | 50.66 | 63.17 | 79.87 | 100.06 | 124.76 | 143.90 | 158.11 | 162.17 | 156.01 | 141.43 |
| 1.25 | 4.45 | 6.32 | 8.93 | 12.10 | 17.99 | 25.38 | 30.25 | 34.32 | 40.57 | 48.63 | 58.96 | 72.37 | 87.10 | 104.45 | 114.38 | 117.90 | 112.99 | 100.36 | 82.98 |
| 1.48 | 4.43 | 6.27 | 8.81 | 11.89 | 17.58 | 25.31 | 29.24 | 32.76 | 38.22 | 45.08 | 53.68 | 64.17 | 74.27 | 84.98 | 87.37 | 82.49 | 71.72 | 56.78 | 41.65 |
| 1.76 | 4.40 | 6.22 | 8.77 | 11.84 | 17.49 | 24.55 | 28.77 | 31.79 | 36.45 | 41.70 | 47.84 | 54.59 | 59.69 | 64.30 | 61.04 | 52.71 | 42.15 | 31.37 | 23.24 |
| 2.08 | 4.36 | 6.15 | 8.63 | 11.57 | 17.00 | 24.38 | 27.39 | 29.67 | 33.23 | 36.99 | 41.16 | 44.85 | 45.95 | 45.95 | 39.13 | 30.00 | 21.82 | 16.03 | 13.45 |
| 2.47 | 4.34 | 6.11 | 8.56 | 11.46 | 16.81 | 23.52 | 26.52 | 28.06 | 30.44 | 32.41 | 34.10 | 34.85 | 32.98 | 30.55 | 23.81 | 17.43 | 13.15 | 10.81 | 9.97 |
| 2.93 | 4.28 | 6.00 | 8.33 | 11.06 | 16.09 | 23.17 | 24.54 | 25.16 | 26.23 | 26.70 | 26.74 | 25.53 | 22.00 | 18.54 | 13.35 | 10.01 | 8.43 | 7.59 | 7.04 |
| 3.48 | 4.21 | 5.87 | 8.12 | 10.72 | 15.54 | 21.88 | 22.78 | 22.41 | 22.24 | 21.24 | 19.89 | 17.69 | 14.15 | 11.54 | 8.65 | 7.20 | 6.35 | 5.60 | 5.03 |
| 4.12 | 4.11 | 5.68 | 7.78 | 10.10 | 14.42 | 20.94 | 20.02 | 18.64 | 17.34 | 15.48 | 13.59 | 11.15 | 8.31 | 6.97 | 5.81 | 5.22 | 4.57 | 3.94 | 3.52 |
| 4.89 | 3.98 | 5.45 | 7.41 | 9.49 | 13.44 | 19.02 | 17.50 | 15.29 | 13.22 | 11.00 | 9.19 | 7.25 | 5.46 | 5.01 | 4.44 | 3.92 | 3.39 | 2.96 | 2.66 |
| 5.80 | 3.80 | 5.13 | 6.85 | 8.56 | 11.89 | 17.41 | 14.34 | 11.59 | 9.19 | 7.28 | 5.88 | 4.64 | 3.77 | 3.72 | 3.29 | 2.88 | 2.52 | 2.23 | 2.05 |
| 6.88 | 3.62 | 4.81 | 6.32 | 7.72 | 10.54 | 14.98 | 11.55 | 9.27 | 7.28 | 5.88 | 4.64 | 3.77 | 3.25 | 2.84 | 2.50 | 2.22 | 1.96 | 1.74 | 1.62 |
| 8.15 | 3.40 | 4.40 | 5.65 | 6.67 | 8.90 | 10.60 | 8.47 | 6.22 | 4.76 | 3.94 | 2.96 | 2.53 | 2.24 | 2.21 | 1.97 | 1.77 | 1.57 | 1.42 | 1.32 |
| 9.66 | 3.13 | 3.93 | 4.90 | 5.57 | 7.27 | 8.42 | 6.66 | 4.24 | 3.16 | 2.70 | 2.31 | 1.99 | 1.75 | 1.75 | 1.58 | 1.44 | 1.29 | 1.16 | 1.08 |
| 11.44 | 2.79 | 3.38 | 4.08 | 4.47 | 5.75 | 6.58 | 5.03 | 3.19 | 2.54 | 2.21 | 1.88 | 1.61 | 1.41 | 1.45 | 1.31 | 1.20 | 1.09 | 0.98 | 0.94 |
| 13.55 | 2.30 | 2.73 | 3.21 | 3.37 | 4.32 | 4.97 | 3.80 | 2.48 | 2.05 | 1.75 | 1.50 | 1.28 | 1.13 | 1.18 | 1.07 | 1.00 | 0.92 | 0.84 | 0.81 |
| 16.02 | 1.73 | 2.02 | 2.35 | 2.34 | 3.03 | 3.60 | 2.86 | 1.94 | 1.60 | 1.37 | 1.20 | 1.02 | 0.90 | 0.93 | 0.84 | 0.80 | 0.75 | 0.70 | 0.66 |

**Acknowledgments**